THE ASTROPHYSICAL JOURNAL, 560:763–771, 2001 October 20


# SHOCK WAVE EMISSION AT MILLER'S POSITION 1 IN THE CYGNUS LOOP

J. C. RAYMOND AND J. LI[1]
Harvard-Smithsonian Center for Astrophysics, Cambridge, MA 02138
WILLIAM P. BLAIR
Department of Physics and Astronomy, Johns Hopkins University, Charles and 34th Streets, Baltimore, MD 21218
AND
ROBERT H. CORNETT
Raytheon STX Corporation, Code 681, NASA/Goddard Space Flight Center, Greenbelt, MD 20771
*Received 1999 January 15; accepted 2001 June 21*

## ABSTRACT

We present the far-UV spectrum (900–1800 Å) of the bright filament known as Miller's (1974) position 1 in the Cygnus Loop obtained with the Hopkins Ultraviolet Telescope during the Astro-2 space shuttle mission. Longer wavelength *IUE* and ground-based spectra of adjoining regions were scaled to produce a combined spectrum ranging from 900 to 7500 Å. We compare this spectrum with models of radiative shock waves to infer shock velocities and elemental abundances. A power-law distribution of shock velocities within the spectrograph apertures can reproduce the observed spectrum. We consider the question of whether a simpler shock structure, thermally unstable cooling, or a mixing layer could produce a similar spectrum. We also discuss the elemental abundances with particular attention to C and Si, whose lines are only available in the UV.

*Subject headings:* ISM: individual (Cygnus Loop) — shock waves — supernova remnants — ultraviolet: ISM

## 1. INTRODUCTION

The Cygnus Loop is a bright supernova remnant (SNR) that was probably formed by a stellar explosion in a relatively low density region of the interstellar medium (ISM). Because it is nearby and relatively unreddened, it has been extensively studied as the classic "middle-aged" SNR. In some regions the blast wave appears in X-ray emission accompanied by little if any optical nebulosity. The areas where the blast wave encounters dense clouds, possibly a shell formed by the SN progenitor, are regions where the radiative shocks produce bright optical and UV emission (e.g., Shull et al. 1985; Hester, Raymond, & Blair 1994; Levenson et al. 1997). The optical size of the Cygnus Loop is approximately $160' \times 210'$. The canonical distance estimate of 770 pc was recently revised to 440 pc based on a *Hubble Space Telescope* proper motion study (Blair et al. 1999).

A wide range of shock velocities can occur in an SNR. A complete spectrum provides information on a range of shock velocities, along with elemental abundances, densities, and preshock ionization state. A fast shock heats the surrounding gas to high temperature (Cox 1972a), which gives rise to high-ionization stages. Few lines of highly ionized species are available in the optical range, so UV spectra are especially important for estimating shock speeds.

In this paper, we present new observations of position 1 of Miller (1974) in the Cygnus Loop from the Hopkins Ultraviolet Telescope (HUT) covering the 912–1840 Å wavelength range. In contrast to the Cygnus Loop regions observed by HUT during the Astro-1 mission (Blair et al. 1991; Long et al. 1992), this is a region where the shocked gas seems to have completely cooled and recombined. Miller's position 1 is one of the brightest regions in the Cygnus Loop at optical wavelengths, and it therefore provides a high-quality spectrum. We combine the HUT spectrum with *IUE* spectra at longer UV wavelengths and with Miller's optical spectrum. A UV image from the Ultraviolet Imaging Telescope (UIT) provides the context for the spectral data. We find that no single shock speed matches the spectrum but that a distribution of shock velocities between about 60 and 200 km $s^{-1}$ can explain the observations to within the uncertainties of model calculations. We discuss the possibilities that thermal instability or a range of preshock densities cause the spread in shock velocity. Carbon or silicon may be depleted but only at the 30% level, suggesting that grain destruction in the shocked gas has been fairly effective.

## 2. DATA REDUCTION

The data analyzed in this paper all pertain to a bright radiative region of filaments in the northeast Cygnus Loop that was first observed by Miller (1974) as his "position 1." Below we discuss the new data sets we have obtained and then describe how they have been combined with existing data on this region. A summary of positions, apertures, position angles, and wavelength coverage for the spectrographic data is given in Table 1.

### 2.1. *New Data*

The new data were obtained on the Astro-2 space shuttle mission in 1995 March, using two telescopes in the Astro Observatory package. The spectrum from 900 to 1800 Å was obtained using the HUT as part of a guest investigator program. Simultaneously, the coaligned UIT was exposed,

[1] Visiting Scientist, Smithsonian Astrophysical Observatory.

TABLE 1

SUMMARY OF UV AND OPTICAL SPECTROGRAPHS

| Instrument | R.A. (B1950) | Decl. (B1950) | Aperture Size (arcsec × arcsec) | Position Angle (deg) | Spectral Resolution (Å) | Wavelength Coverage (Å) |
|---|---|---|---|---|---|---|
| HUT 1..... | 20 54 15.0 | +31 32 48 | 10 × 56 | 90 | 3.5 | 820–1840 |
| HUT 2..... | 20 54 15.0 | +31 33 18 | 10 × 56 | 90 | 3.5 | 820–1840 |
| *IUE* SWP ..... | 20 54 15.0 | +31 32 59 | 10 × 20 | 172 | 10 | 1150–1950 |
| *IUE* LWR..... | 20 54 15.0 | +31 32 59 | 10 × 20 | 145 | 10 | 1900–3200 |
| Scanner ..... | 20 54 17.8 | +31 33 11 | 2.7 × 68 | 81 | 2.0 ~ 16.4 | 3400–5100 |

NOTE.—Units of right ascension are hours, minutes, and seconds, and units of declination are degrees, arcminutes, and arcseconds.

obtaining a far-ultraviolet (FUV) image roughly centered on the HUT aperture. These data sets are described in more detail below.

The UIT image of the northeast Cygnus Loop was obtained with the B5 filter, which passes the 1450–1800 Å region, with an integration time of 500 s. UIT images a full field of 40′ onto Eastman Kodak IIa-O film, intensified by a CsI photocathode. The film was developed on return to Earth and carefully digitized. The data are then corrected for S-distortion to provide a nearly rectilinear resulting image. Resolution depends on the pointing accuracy during the exposure but is usually in the 2″–3″ range. Since there are very few stars in the FUV bandpass, the astrometry is only good to 5″–10″ for this region. An error in the UIT center position would move all the derived aperture positions in the same manner. The UIT image of this region is discussed and compared with [O III], Hα and X-ray images by Danforth et al. (2000). More details about the UIT telescope and its performance can be found in Stecher et al. (1992). The inner 10′ region of the final B5 image is reproduced in Figure 1. The aperture overlays in this figure will be discussed below. For comparison, a section of the [O III] image provided by Nancy Levenson (Levenson et al. 1998) is shown in Figure 2.

The HUT spectrum covers the 820–1840 Å range in the first order with 0.51 Å per pixel and 3–4 Å spectral resolution (Kruk et al. 1995). Because the region was known to be bright in the UV, two HUT spectra were obtained during a single shuttle pointing: the 10″ × 56″ aperture was placed east-west at the lower of the two matched rectangles in Figure 1 and exposed for 18 minutes, then offset 30″ due north (Fig. 1, *upper rectangle*) and exposed for 13.3 minutes. (Note that the HUT positions lie north and south of Miller's slit.) Unfortunately, the Cygnus Loop was placed solidly in the day portion of the orbit during Astro-2, so airglow emissions are problematic. Upon inspection, the differences between the two spectra, aside from the level of airglow and a 30% higher overall brightness in the northern exposure, are so slight that we have combined them to improve the signal-to-noise ratio. This also indicates that the relative FUV line intensities are not varying widely throughout the region, which is important since the apertures of the various instruments do not coincide exactly.

The HUT data have been reduced using a standardized reduction package developed for HUT data reductions at Johns Hopkins University. The radiometric calibration based on laboratory measurements and on spectra of hot white dwarfs is accurate to better than 5% (Kruk et al. 1995). Since the data are digital, an error array is carried through the reduction process, permitting quantitative fitting of the spectral features. The resulting spectrum is shown in Figure 3*a*. The Earth symbol denotes regions of strong airglow emission.

The line intensities were measured using a nonlinear $\chi^2$-minimization technique programmed as an IRAF task called SPECFIT (Kriss 1994), which permits more accurate flux measurements of blended lines. The line fluxes were extracted by fitting Gaussian profiles. SPECFIT makes it possible to fit fine structure spectral lines with fixed wavelength separations and relative intensities (especially useful for the 1400 Å blend). It was also useful in separating the blend of the O VI doublet ($\lambda\lambda$1032, 1038) from airglow lines Ly$\beta$ and O I ($\lambda\lambda$1026, 1041), and the blend of N V from airglow Ly$\alpha$. We note that a second-order O II airglow line at 834 Å is badly blended with O III] ($\lambda\lambda$1662, 1666). However, because the relative sensitivity of first and second orders has been calibrated and because the shorter wavelength line of the doublet is visible separately in HUT data, we can actually recover the O III] line flux.

We treated the intercombination lines under assumption that the gas has very low density (typically 100 cm$^{-3}$).

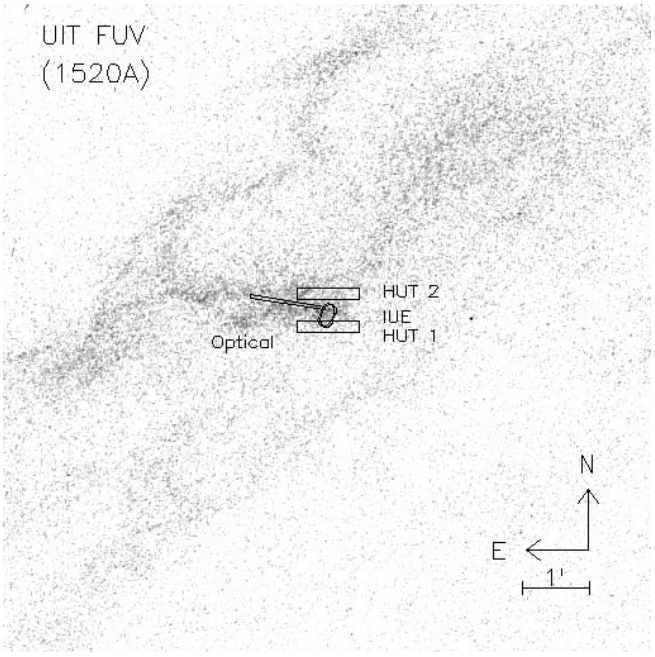


FIG. 1.—A 10′ square portion of the UIT FUV image of the Cygnus Loop, centered at ($\alpha_{1950} = 20^h54^m16^s$ and $\delta_{1950} = +31°32'\ 37''$). North is up, and east is at left. Spectrograph apertures are outlined in black. The two equal-sized HUT apertures (10″ × 56″) flank the oval 10″ × 20″ *IUE* apertures (Benvenuti et al. 1980; D'Odorico et al. 1980) to the north and south. Miller's (1974) optical-band aperture (2.″7 × 68″) lies along the filament to the east.

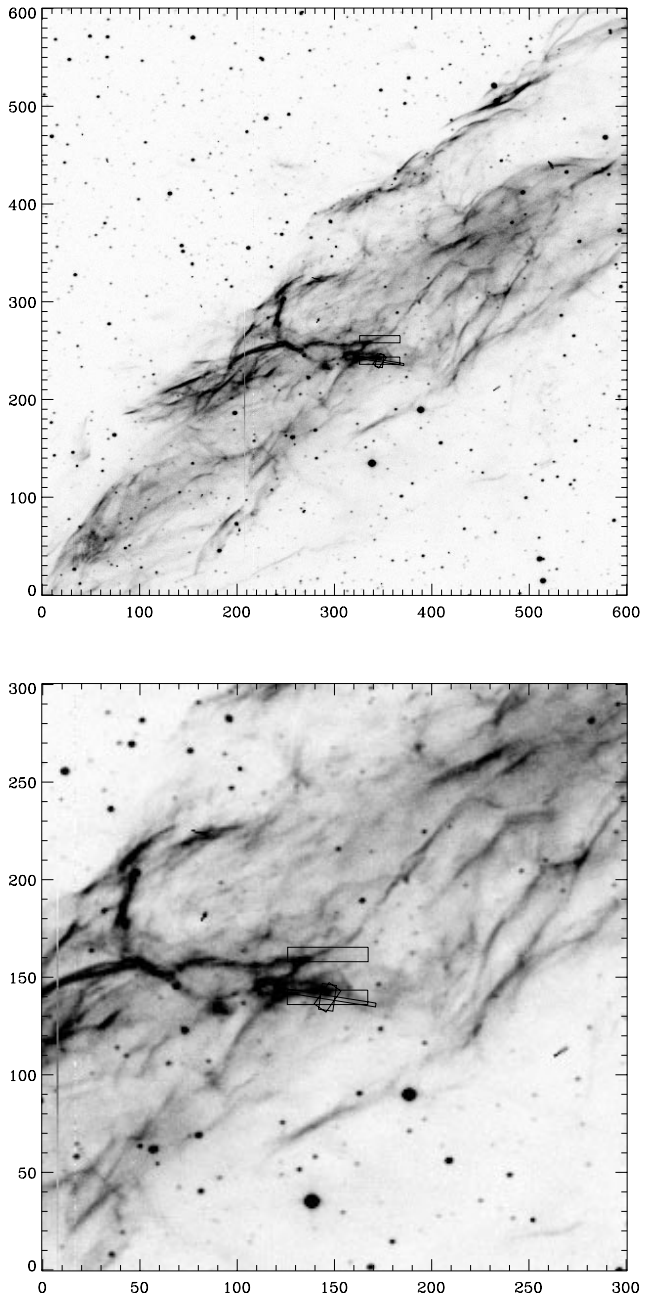

FIG. 2.—Narrowband images in [O III] λ5007 from Levenson et al. (1998). The upper and lower images are approximately 13.5 and 6.75 on a side, respectively.

Under this condition, the intensity ratios among the components of each multiplet depend on their collision strengths from ground level and branching ratios. The resonance doublets of C IV, N V, Si IV, and O VI have intrinsic intensity ratios of 2:1, but scattering in the emitting gas or in the intervening ISM will affect the brighter line of the doublet more strongly. Therefore, we did not fix these intensity ratios. The flux uncertainties include the fitting errors given by SPECFIT and a conservative 10% for radiometric calibration accuracy. Table 2 lists the emission lines measured from the HUT spectrum and their uncertainties. Above 1800 Å, the spectrum is contaminated by the airglow blend from 900 Å in second order.

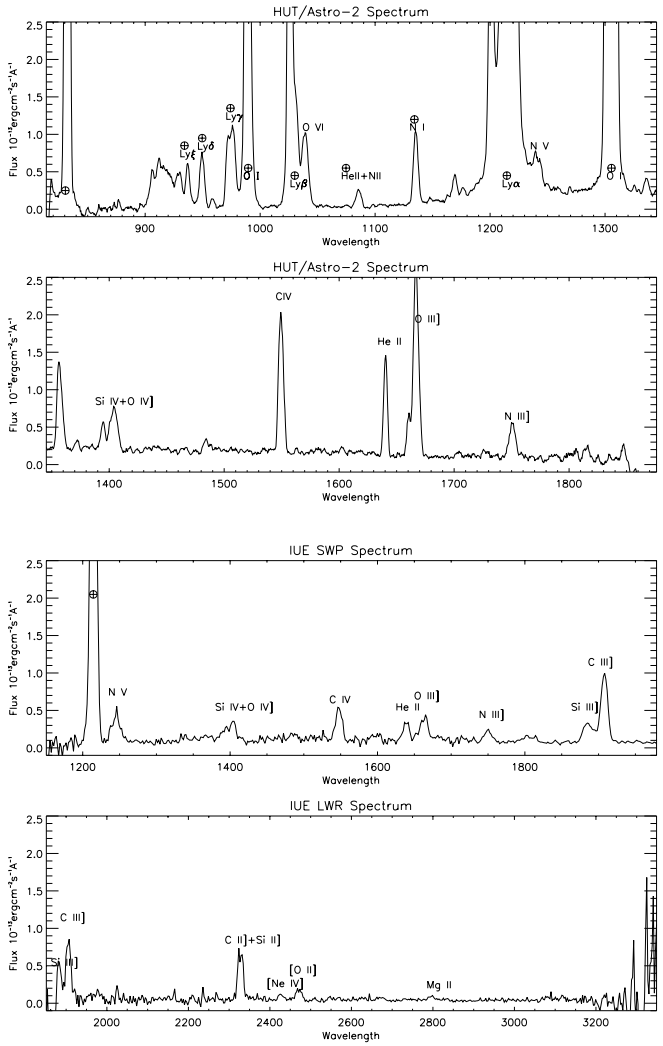


FIG. 3.—(*a*) Calibrated FUV spectrum of Miller's position 1 in the Cygnus Loop from HUT/Astro-2 obtained in 1995 March. Major lines are marked, and the Earth symbol denotes regions of airglow contamination. (*b*) The reextracted UV spectra from *IUE* for Miller's position 1.

TABLE 2

EMISSION LINES FROM CYGNUS LOOP POSITION 1 OBSERVED BY HUT/ASTRO-2

| IONS | WAVELENGTH (Å) | FLUX ($\times 10^{-13}$ ergs cm$^{-2}$ s$^{-1}$) Observed | Dereddened |
|---|---|---|---|
| C III ..... | 977 | 1.67 ± 0.34 | 5.97 ± 1.20 |
| O VI ..... | 1035 | 9.06 ± 1.10 | 27.19 ± 3.30 |
| C III] ..... | 1175 | 0.60 ± 0.22 | 1.40 ± 0.52 |
| N V ..... | 1240 | 3.68 ± 0.52 | 7.97 ± 1.12 |
| C II ..... | 1335 | 0.73 ± 0.28 | 1.45 ± 0.56 |
| O V ..... | 1371 | 0.36 ± 0.05 | 0.70 ± 0.09 |
| Si IV ..... | 1396 | 2.04 ± 0.33 | 3.91 ± 0.64 |
| O IV] ..... | 1404 | 3.47 ± 0.39 | 6.62 ± 0.74 |
| N IV] ..... | 1485 | 0.96 ± 0.14 | 1.77 ± 0.25 |
| C IV ..... | 1550 | 9.64 ± 1.17 | 17.48 ± 2.13 |
| [Ne IV] ..... | 1601 | 1.34 ± 0.30 | 2.40 ± 0.55 |
| He II ..... | 1640 | 4.59 ± 1.00 | 8.19 ± 1.76 |
| O III] ..... | 1664 | 8.20 ± 0.96 | 14.59 ± 1.71 |
| N III] ..... | 1750 | 3.16 ± 0.34 | 5.60 ± 0.60 |

The measured fluxes were corrected for extinction based on a reddening of $E(B-V) = 0.08$ for the Cygnus Loop (Parker 1967) and the reddening curves derived by Cardelli, Clayton, & Mathis (1989). The fractional errors for the reddening corrections were considered to be proportional to the ratios of dereddened fluxes to the observed fluxes and are also listed in Table 2.

### 2.2. *Existing Data*

The UV spectrum of Miller's position 1 from 1200 to 3200 Å as obtained with *IUE* has been published previously (Benvenuti et al. 1980; D'Odorico et al. 1980). The *IUE* aperture positions are shown superposed on the UIT image in Figure 1. Benvenuti, D'Odorico, & Dopita (1980) tried to choose the *IUE* positions to match Miller's optical spectrum, but Miller did not provide coordinates. The positions indicated in Table 1 and Figure 1 are based on the coordinates listed in the *IUE* archival spectra and the position of Miller's guide star (star "a" in his finding chart). We have remeasured fluxes from these spectra (SWP 1327 and LWR 6306) to take advantage of the improved radiometric calibration and extraction techniques of the Final Archive. In particular, the optimal extraction technique seems to do a good job of removing the particle event that contaminated the C II λ1335 line in SWP 1327. Figure 3*b* shows the *IUE* spectra. The measured fluxes and their uncertainties are given in Table 3. The dereddened fluxes were obtained through the same process as used with the HUT data.

The optical spectrum (Miller 1974) was obtained with a prime-focus scanner attached to the 3 m telescope at Lick Observatory. The reconstructed position of Miller's slit compared to the other apertures is also shown on Figure 1. The position of the optical long slit aperture on the UV nebulosity matches with the position of the slit in Miller's finding chart. It is about 30″ east and 23″ north of the *IUE* position. We adopt Miller's observed fluxes before the reddening correction and, for consistency, dereddened the fluxes with the same reddening curves used above. Miller quotes uncertainties of 10% for strong lines [$F(\lambda) \geq 0.5F(H_\beta)$], 25% for lines of intermediate strength with $0.5F(H_\beta) \leq F(\lambda) \geq 0.1F(H_\beta)$, and 50% for weak lines [$F(\lambda) \leq 0.1F(H_\beta)$; see Miller 1974].

TABLE 3

EMISSION LINES FROM CYGNUS LOOP POSITION 1 OBSERVED BY *IUE*

| IONS | WAVELENGTH (Å) | CAMERA | FLUX ($\times 10^{-13}$ ergs cm$^{-2}$ s$^{-1}$) Observed | Dereddened |
|---|---|---|---|---|
| N V ..... | 1240 | SWP | 5.89 ± 0.78 | 12.76 ± 1.69 |
| Si IV ..... | 1396 | SWP | 1.84 ± 0.74 | 3.53 ± 1.42 |
| O IV] ..... | 1404 | SWP | 2.08 ± 0.64 | 3.97 ± 1.22 |
| C IV ..... | 1550 | SWP | 4.36 ± 0.55 | 7.90 ± 1.00 |
| He II..... | 1640 | SWP | 2.35 ± 0.42 | 4.19 ± 0.75 |
| O III] ..... | 1664 | SWP | 4.13 ± 0.53 | 7.34 ± 0.94 |
| N III] ..... | 1750 | SWP | 1.70 ± 0.32 | 3.01 ± 0.57 |
| Si III] ..... | 1890 | SWP | 4.27 ± 0.13 | 7.73 ± 0.24 |
| C III] ..... | 1909 | SWP | 10.39 ± 0.12 | 18.94 ± 0.22 |
| C II] ..... | 2325 | LWR | 4.89 ± 0.62 | 9.22 ± 1.17 |
| Si II]..... | 2335 | LWR | 2.62 ± 1.03 | 4.91 ± 1.93 |
| [Ne IV]... | 2420 | LWR | 0.76 ± 0.24 | 1.34 ± 0.42 |
| [O II] .... | 2470 | LWR | 1.78 ± 0.32 | 3.07 ± 0.55 |
| Mg II ..... | 2802 | LWR | 1.06 ± 0.21 | 1.65 ± 0.33 |

### 2.3. *Combined Data Set*

There are some obvious potential difficulties in combining these disparate data sets. The projected aperture areas of the UV spectrographs were similar, but the aperture shapes, positions, and orientations differ. For instance, the HUT and optical slit orientations were aligned along the bright filament, and the long axes of the *IUE* SWP and LWR slits on *IUE* were both aligned roughly perpendicular to the filament. However, as demonstrated by the two HUT spectra, the relative line intensities across the region seem to be fairly constant. Hence, we proceed by producing a normalized data set that corrects for these differences.

The UV spectral lines were normalized to the O III] λ1664 for both HUT and *IUE* short-wavelength observations. To put the *IUE* long-wavelength spectrum on the same scale, we normalized the long-wavelength spectrum to C III] λ1909 line, which is present in both short- and long-wavelength spectra. To scale the optical spectrum to the UV, we use the relative intensities in [O III] λ5007 obtained from the image in Figure 2, scaling Miller's spectrum to the average [O III] intensities of the two HUT apertures. Miller placed the narrow spectrograph aperture directly along the bright filament, while the HUT aperture encompasses both bright and faint regions. The average surface brightness within Miller's aperture is 2.19 times that in the southern HUT aperture. The resulting UV to optical intensity ratios are 15% smaller than would be obtained by assuming that the intensity ratio $I(\lambda5007 + \lambda4959)/I(\lambda1664)$ is 2.6, as predicted by shock models in Table 5, the procedure adopted by, for instance, Raymond et al. (1997).

The uncertainties in relative intensities of all the lines were calculated through propagation of errors. Table 4 gives line intensities relative to O III] λ1664 and the uncertainties. The uncertainty estimate does not include the possibility that very different regions fell within the apertures of the different instruments, which is difficult to quantify. A useful check is a comparison of the [O III] λ5007 intensities within the HUT and *IUE* apertures as obtained from the narrowband [O III] image in Figure 2. The northern HUT aperture shows an [O III] λ5007 91% that of the southern aperture, while the O III] λ1664 is 29% larger. The *IUE* SWP aperture has an [O III] λ5007 surface brightness 12% higher than the southern HUT aperture, while the O III] λ1664 surface brightness is 67% higher. This comparison is dominated by the uncertainty in the exact position of the *IUE* slit, which was based on a blind offset and could easily be comparable to the size of the aperture. Therefore, comparison of optical line fluxes in the HUT and *IUE* apertures is far less reliable than the scaling to the O III] λ1664 flux that the two spectra have in common.

An additional aspect of the combined data set that can be checked is the comparison of spectral fluxes with the UIT flux through the projected apertures, as shown in Figure 1. The UIT spectral fluxes from the various apertures are 1.01, 1.30, 0.63, 0.64, and 0.57 $\times 10^{-14}$ ergs cm$^{-2}$ s$^{-1}$ Å$^{-1}$ for the HUT-1, HUT-2, *IUE* short-wavelength, *IUE* long-wavelength, and optical apertures, respectively. These fluxes are averages over the B5 spectral range of 1450–1800 Å. For comparison, the HUT and *IUE* fluxes integrated over this bandpass are about 50% larger. The discrepancy may be due to a slight misregistration of the UIT, HUT, and *IUE* positions, or it may result from uncertainty in the UIT calibration for the pixels showing very low flux. All in all,

TABLE 4

OBSERVED SPECTRAL LINES WITH DIFFERENT INSTRUMENTS

| Ions | Wavelength (Å) | HUT | *IUE* | Optical[a] |
|---|---|---|---|---|
| O VI ..... | 1035 | 186 ± 31 | ... | ... |
| C III] ..... | 1175 | 10 ± 4 | ... | ... |
| N V ..... | 1240 | 55 ± 10 | 173 ± 32 | ... |
| C II ..... | 1335 | 10 ± 4 | ... | ... |
| O V ..... | 1371 | 5 ± 1 | ... | ... |
| Si IV ..... | 1396 | 27 ± 5 | 48 ± 20 | ... |
| O IV] ..... | 1404 | 45 ± 7 | 54 ± 18 | ... |
| N IV] ..... | 1485 | 12 ± 2 | ... | ... |
| C IV ..... | 1550 | 120 ± 20 | 108 ± 19 | ... |
| [Ne IV] ..... | 1601 | 16 ± 4 | ... | ... |
| He II ..... | 1640 | 56 ± 14 | 57 ± 12 | ... |
| O III] ..... | 1664 | 100 ± 17 | 100 ± 18 | ... |
| N III] ..... | 1750 | 38 ± 6 | 41 ± 9 | ... |
| Si III] ..... | 1890 | ... | 105 ± 14 | ... |
| C III] ..... | 1909 | ... | 257 ± 33 | ... |
| C II] ..... | 2325 | ... | 125 ± 23 | ... |
| Si II] ..... | 2335 | ... | 67 ± 28 | ... |
| [Ne IV] ..... | 2420 | ... | 18 ± 6 | ... |
| [O II] ..... | 2470 | ... | 42 ± 9 | ... |
| Mg II ..... | 2802 | ... | 23 ± 5 | ... |
| [O II] ..... | 3727 | ... | ... | 645 ± 247 |
| [Ne III] ..... | 3869 | ... | ... | 39 ± 15 |
| [S II] ..... | 4070 | ... | ... | 10 ± 5 |
| [O III] ..... | 4363 | ... | ... | 12 ± 6 |
| He II ..... | 4686 | ... | ... | 3 ± 2 |
| $H_\beta$ ..... | 4861 | ... | ... | 49 ± 19 |
| [O III] ..... | 5000 | ... | ... | 218 ± 46 |
| [N II] ..... | 5755 | ... | ... | 4 ± 3 |
| He I ..... | 5876 | ... | ... | 5 ± 3 |
| [O I] ..... | 6320 | ... | ... | 30 ± 7 |
| [N II] ..... | 6548 | ... | ... | 44 ± 15 |
| $H_\alpha$ ..... | 6563 | ... | ... | 152 ± 58 |
| [N II] ..... | 6584 | ... | ... | 126 ± 51 |
| [S II] ..... | 6720 | ... | ... | 140 ± 27 |
| [O II] ..... | 7325 | ... | ... | 26 ± 10 |

NOTE.—The line intensities are normalized to O III] = 100; $I_{\rm O\,III]} = 8.2 \times 10^{-13}$ ergs cm$^{-2}$ s$^{-1}$.

[a] Miller 1974.

we believe that the normalization of the spectra to each other should be reliable to about ±20%.

Benvenuti et al. (1980) attributed the continuum detected in the *IUE* spectrum to hydrogen two-photon emission, possibly supplemented by CO fluorescent emission. We remeasured the UV continuum from *IUE* spectra and measured the continuum from the HUT spectrum. After subtraction of the wings of the airglow Ly$\alpha$ emission, the HUT spectrum does resemble the theoretical two-photon flux curve, with a peak in the 1400–1500 Å range of $1.7 \times 10^{-14}$ ergs cm$^{-2}$ s$^{-1}$ for the average of the HUT-1 and HUT-2 spectra. The corresponding flux level in the *IUE* spectrum is $1.0 \times 10^{-14}$ ergs cm$^{-2}$ s$^{-1}$, which is consistent with the 3 times larger aperture size of the HUT observation and the more central placement of the *IUE* aperture on the filament. Thus, we confirm the identification of the UV continuum as hydrogen two-photon emission. We see no evidence for molecular fluorescence, but the strong airglow emission would make it difficult to detect fluorescent lines. Benvenuti et al. (1980) attributed the high two-photon to H$\beta$ ratio to collisional excitation of neutral hydrogen atoms in the ionization zone just behind the shock. After correcting for reddening, the HUT two-photon intensity is 15 times H$\beta$. This agrees with the prediction of the model discussed below for a 60 km s$^{-1}$ in nearly neutral gas. It will lead us to favor the "equilibrium" model over the "preionized" model below.

## 3. ANALYSIS

### 3.1. *Comparison of Normalized Spectrum to the Shock Wave Models*

Shock models were computed following the methods described by Cox (1972c) and Raymond (1979). They are similar to the models of Hartigan, Raymond, & Hartmann (1987) except for a few updated atomic rates and preshock conditions more appropriate to the Cygnus Loop— $n_0 = 10$ cm$^{-3}$ and a transverse magnetic field $B_0 = 5$ $\mu$G. The model code predicts fluxes in general agreement with those of Dopita & Sutherland (1996), but we do not include any contribution from the preshock photoionization zone. While this precursor radiation is an important contribution to the intensities of some optical lines in the spectra of extragalactic SNRs (e.g., Vancura et al. 1992a), it is spread over a much larger region than the spectrograph apertures used for the present observations. Models were computed for fully preionized gas and for gas whose ionization state is determined by the ionizing flux produced by the shock (equilibrium preionization). Elemental abundances were taken to be 12:10.93:8.52:7.96:8.82:7.92:7.40:7.60:7.20:7.50 for H:He:C:N:O:Ne:Mg:Si:S:Fe, respectively (Allen 1973). The models were run until the gas cooled to 630 K, at which point it has stopped producing significant optical and UV emission.

We first assessed single velocity shock models by minimizing the $\chi^2$ of the difference between a model and the observed relative fluxes. This procedure does not account for the variation in the confidence with which different lines are predicted by the models or for the uncertainty in scaling the spectra from the different instruments, but it gives a relatively systematic way to choose among models. Column (4) of Table 5 shows the model for a single shock velocity, 120 km s$^{-1}$. It is clearly a poor fit. The difficulty is that a shock faster than 160 km s$^{-1}$ is needed to produce any O VI emission at all, but a shock this fast does a poor job of matching the optical spectrum.

We next considered models in which a range of shock velocities is assumed to be present within the patch of sky falling within the spectrograph aperture. We modeled the observed spectrum with a power-law velocity distribution (following Vancura et al. 1992a). The ram pressure is assumed constant everywhere, and so the density is proportional to the inverse shock velocity squared ($n_0 \propto 1/v_s^2$). The observed area covered by shocks with velocity $v_s$ is proportional to $(v_s/100)^p$. The shock model with mixed shock velocities was constructed as

$$I(\lambda, p) \propto \sum I\left[\lambda, \left(\frac{v_s}{100}\right)^p \times \left(\frac{v_{s0}}{v_s}\right)^2\right], \quad (1)$$

where $v_s$ is the shock velocity, $v_{s0}$ is the reference shock velocity, which was 60 km s$^{-1}$ in the calculation, and the summation runs over models spaced by 20 km s$^{-1}$ in shock speed. The value of $p$ controls the relative contributions from fast and slow shocks to the final shock model. The observed spectrum was compared with the model spectrum as the slope $p$ varied. The $\chi^2$ estimation is applied with

TABLE 5

OBSERVED FLUXES AND PREDICTED SPECTRUM BY SHOCK MODELS

| Ions (1) | Wavelength (Å) (2) | Observed Flux (3) | Single Velocity Shock Model[a] (120 km s$^{-1}$) (4) | Equilibrium Preionization Model[b] (60 ~ 200 km s$^{-1}$) (5) | Complete Preonization Model[c] (60 ~ 200 km s$^{-1}$) (6) |
|---|---|---|---|---|---|
| O VI ..... | 1035 | 186 | 0 | 407 | 217 |
| C III] ..... | 1175 | 10 | 11 | 8 | 9 |
| N V ..... | 1240 | 55 | 14 | 74 | 38 |
| O V ..... | 1371 | 5 | 0 | 8 | 4 |
| Si IV ..... | 1396 | 27 | 39 | 52 | 67 |
| O IV] ..... | 1404 | 45 | 88 | 103 | 65 |
| N IV] ..... | 1485 | 12 | 28 | 26 | 17 |
| C IV ..... | 1550 | 120 | 650 | 387 | 239 |
| He II ..... | 1640 | 56 | 59 | 37 | 22 |
| O III] ..... | 1664 | 100 | 100 | 100 | 100 |
| N III] ..... | 1750 | 38 | 38 | 34 | 38 |
| Si III] ..... | 1890 | 105 | 47 | 61 | 132 |
| C III] ..... | 1909 | 258 | 328 | 256 | 359 |
| C II] ..... | 2325 | 126 | 125 | 131 | 200 |
| Si II] ..... | 2335 | 67 | 3 | 6 | 5 |
| [Ne IV] ... | 2420 | 18 | 27 | 26 | 16 |
| [O II] .... | 2470 | 42 | 11 | 13 | 21 |
| Mg II ..... | 2802 | 23 | 24 | 69 | 34 |
| [O II] .... | 3727 | 645 | 322 | 436 | 601 |
| [Ne III] ... | 3869 | 39 | 18 | 18 | 27 |
| [S II] ..... | 4070 | 10 | 6 | 10 | 9 |
| [O III] .... | 4363 | 12 | 16 | 16 | 16 |
| He II ..... | 4686 | 3 | 5 | 3 | 2 |
| $H_\beta$ ..... | 4861 | 49 | 43 | 150 | 58 |
| [O III] .... | 5000 | 218 | 262 | 237 | 260 |
| [N II] .... | 5755 | 4 | 2 | 3 | 3 |
| He I ..... | 5876 | 5 | 5 | 5 | 7 |
| [O I] ..... | 6320 | 30 | 9 | 32 | 10 |
| [N II] .... | 6548 | 44 | 18 | 30 | 25 |
| $H_\alpha$ ..... | 6563 | 152 | 132 | 477 | 183 |
| [N II] .... | 6584 | 126 | 53 | 91 | 76 |
| [S II] ..... | 6720 | 140 | 91 | 182 | 136 |
| [O II] .... | 7325 | 26 | 15 | 18 | 28 |

[a] The model is computed from a single shock velocity.

[b] The combined shock models with shock velocities ranging from 60 to 200 km s$^{-1}$ under the assumption of equilibrium preionization. The line intensities were assembled with eq. (1).

[c] Shock models for complete preionization are adopted. The line intensities were assembled with eq. (1).

respect to $p$ in order to find the best fit between the observational and theoretical spectra,

$$\chi^2(p) = \left\{ \sum \left[ \frac{I_{\rm obs}(\lambda) - I_{\rm mod}(\lambda, p)}{\sigma(\lambda)} \right]^2 \right\} \Big/ N \,, \qquad (2)$$

where $I_{\rm obs}(\lambda)$ stands for observed line intensities as function of wavelength, $\lambda$. $I_{\rm mod}(\lambda, p)$ is the constructed spectrum as function of $p$. Both spectra have been normalized to O III] $\lambda$1664. $N$ is the number of spectral lines included, and $\sigma(\lambda)$ are uncertainties of the observed spectral line intensities, which are derived from the uncertainties given in Table 4. We have assigned large uncertainties to the lines likely to be affected by resonance scattering: C II, C IV, N V, and O VI (Raymond et al. 1980; Cornett et al. 1992). When the shock velocity ranges from 60 to 200 km s$^{-1}$, the $\chi^2$ minimum estimation gave the best fit of $p = -2.38$ for models with the preshock ionization determined by equilibrium with the flux of ionizing photons from the shock. For models with preionized gas $p = -2.09$ gave the best fit. The preshock gas will be more ionized than predicted by the equilibrium models if the shock decelerates rapidly from $V_s \sim 150$ km s$^{-1}$, when it produces intense ionizing radiation, to $V_s \sim 60$ km s$^{-1}$, when it produces few ionizing photons, in a time shorter than the recombination time of the preshock gas (Cox 1972b). This situation has been inferred for the "Spur" filament in the Cygnus Loop (Raymond et al. 1988). Table 5 summarizes the observed spectrum, a single velocity shock model, and constructed spectra with shock velocity ranging from 60 to 200 km s$^{-1}$ for equilibrium preionization and complete preionization models. The comparison of observed to predicted flux is visualized in Figure 4 for the preionized models and for several power-law slopes. The strongest variation with the power-law slope is seen for the O VI line, which is too strong for flat power laws and too faint for steep ones. This demonstrates once again the importance of accessing O VI for typical ISM shocks (see Vancura et al. 1992b). The emission lines do not discriminate between the models with equilibrium preshock ionization and those with preionized gas. However, the former produce strong H I two-photon continuum, and the latter do not. Thus, we favor the equilibrium preionization models or perhaps even models of shocks in underionized gas.

Most of the lines that fall significantly above the Predicted = Observed line in Figure 4 are resonance lines

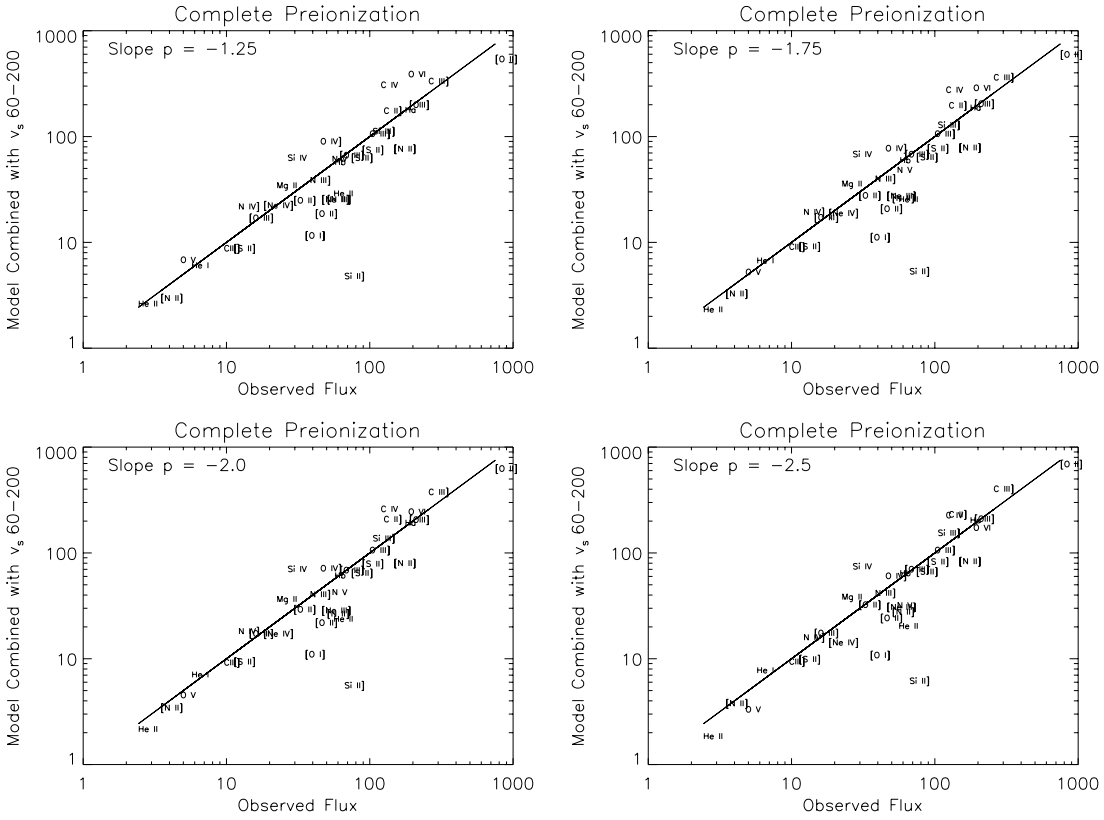


FIG. 4.—Comparison of observed spectral line intensities to the theoretical spectrum constructed from a range of shock velocities from 60 to 200 km $s^{-1}$. Both spectra have been normalized to O III] $\lambda$1664. The solid straight lines represent equality between the observed and modeled line intensities. The four graphs represent different power-law slopes $p$ when the modeled spectra were produced according to eq. (1).

whose brightness will be lower than the model predictions because of scattering both in the emitting filament itself and in the intervening ISM (C IV, Si IV, N V, O VI; Raymond et al. 1988; Cornett et al. 1992; Long et al. 1992). Of the lines predicted to be significantly fainter than the observed values, the Si II] $\lambda$2325 line suffers from a large measurement uncertainty owing to the difficulty in separating it from the stronger adjacent C II] line. The C III $\lambda$1176 line is likewise difficult to measure because it lies in a region of strong airglow emission. The He II $\lambda$4686 recombination line prediction agrees well with the observation, while the $\lambda$1640 line prediction is too small. It may be that the collisional excitation contribution to the $\lambda$1640 intensity is underestimated because the preshock ionization of He has been overestimated or because the collisional excitation rate in the model is underestimated. In general, the predicted fluxes of the lowest ionization lines ([O I], [S II], [N II] and [O II]) are about half the observed values. A power-law model with a steeper slope would do better in this regard but would tend to underpredict the high-ionization lines. The assumption of a power-law distribution of shock speeds may be at fault, but other possibilities include the positional shift between the optical and UV spectrograph apertures or a contribution from shocks even slower than 60 km $s^{-1}$.

The power-law distributions in shock velocity do a fair job of matching the spectra. Shock speeds of at least 180 km $s^{-1}$ are required to produce the O VI emission, and shock speeds below 100 km $s^{-1}$ are required to produce the [O II] $\lambda$3727 intensity (and even these models fall somewhat short of matching the emission in the lowest ionization states, O I and S II). The value of $p$ should not be taken as a meaningful indication of the distribution of shock speeds, because it is sensitive to the fairly arbitrary choice of maximum and minimum shock velocities. Indeed, there is no physical basis for the assumption of a power-law distribution of shock contributions, and the real distribution probably does include stronger emission from the fastest and slowest shocks than we have assumed. However, given the uncertainties and simplifying assumptions used in the shock models, we choose not to add more free parameters to the distribution of shock velocities in an attempt to match the observations further. We conclude that a broad shock velocity distribution is required (at least 80–180 km $s^{-1}$ and probably 60–200 km $s^{-1}$).

It might be possible to explain the spectra with just two shock speeds, one fast and one slow. This could correspond, for instance, to a fast, somewhat face-on shock producing diffuse UV emission over a large region, while a slower shock in denser gas produces the bright filament seen in lower ionization emission lines. To explain the O VI emission with a nonradiative shock, one would require a factor of 100 enhancement over the emission of a face-on shock with the ram pressure derived by Hester et al. (1994). Such a nonradiative shock would help to explain the strong He II $\lambda$1640 emission, but it would overpredict the N V flux. It would also explain the similarity between the two HUT spectra north and south of the optical filament. Images in the [Ne V] $\lambda$3245 line, similar to those obtained by Szentgyorgyi et al. (2000) farther south in the Cygnus Loop, show filamentary emission basically similar to the brightest filaments in Figure 2. While we have not been able to find a combination of two shocks that matches the spectrum, the

uncertainties in the models preclude a strong statement that a broad distribution is needed.

Thus, it is not yet clear whether the shock velocity distribution we observe is connected to the 400 km $s^{-1}$ shocks responsible for the X-ray emission (Ku et al. 1984; Miyata et al. 1994; Levenson et al. 1997). If there are radiative shocks in the 200–300 km $s^{-1}$ range, they emit strongly in both the high-temperature UV lines and the low-ionization lines formed in the recombination zone (see Hartigan et al. 1987). Such shocks may contribute, but they are not required to explain the optical/UV spectrum. Within the context of models for the encounter of a blast wave with a large-scale cloud or dense shell (Hester et al. 1994; Levenson et al. 1996), there is no reason to expect these intermediate shock speeds.

### 3.2. *Elemental Abundances*

One goal of the HUT observation was a measurement of the abundances of carbon and silicon, which have strong UV lines but no strong lines at optical wavelengths. These elements are likely to be depleted onto grains in the preshock gas and gradually liberated from the grains by sputtering and grain-grain collisions in the postshock flow (e.g., Jones, Tielens, & Hollenbach 1996). Shocks are believed to dominate grain destruction in the Galactic disk and therefore to determine the overall grain population in the ISM (Scalo 1977). Jones et al. (1996) find that roughly half the grain material is vaporized behind a 100 km $s^{-1}$ shock. More effective grain destruction is expected in faster shocks.

Comparison of the combined spectrum with the models in Table 5 shows that the 60–200 km $s^{-1}$ model matches the ratios of O IV] to N IV] and N III] to O III] to about 30%, suggesting that the model gives a good representation of the ionization structure in the neighborhood of $3 \times 10^4$ to $1.5 \times 10^5$ K. The C IV and Si IV lines are about $\frac{2}{3}$ as bright as the model prediction, but that is likely to be a result of resonance scattering either in the filament or in the intervening ISM. The C III] line is roughly $\frac{2}{3}$ as bright as expected, and the Si III] line matches the predicted flux. Thus, the data suggest that C and Si are undepleted in the shocked gas with an uncertainty of about 30%. This is consistent with the predictions of the Jones et al. (1994) model, considering that much of the UV emission arises from shocks faster than 100 km $s^{-1}$ that probably destroy grains quite effectively. Jones et al. (1996) found that grain-grain collisions did not return dust material to the gas phase very effectively and that most of these collisions occur in the relatively cool portion of the flow where the compression is high. Thus, any material liberated by grain-grain collisions would probably not be represented in the UV line emission.

### 3.3. *Ram Pressure and Length Scale*

The brightness of the region observed is given by the product of the intrinsic emission per square centimeter of the shock and the depth of the filament along the line of sight (within the aperture of the spectrograph). The intrinsic emission is

$$I = \frac{v_s n_0 N h\nu}{4\pi} \text{ ergs cm}^{-2} \text{ s}^{-1} \text{ sr}^{-1} , \quad (3)$$

where the shock velocity times $n_0$ gives the number of atoms per square centimeter per second swept up by the shock, $h\nu$ is the photon energy, and $N$ is the number of photons emitted in a given line per atom passing through the shock. For [O III] $\lambda$5007, $N$ is about 0.55 (Raymond et al. 1988). The observed O III] flux in the HUT aperture and the [O III] / O III] scaling imply

$$n_0 v_7 l \simeq 3.1 \text{ cm}^{-3} \text{ pc} , \quad (4)$$

where $v_7$ is the shock speed in units of 100 km $s^{-1}$ and $l$ is the depth of the filament along the line of sight in a region corresponding to the 11″ HUT slit width. For $v_7 \simeq 1.2$, near the middle of the shock speed range inferred above and a ram pressure on the order of that of the blast wave (intercloud density $\simeq 0.2$ $cm^{-3}$; Ku et al. 1984), the line-of-sight depth is on the order of 1.5 pc. The full width of the filament on the sky is about 4 times the width of the HUT aperture, so the filament extends 5–6 pc along the line of sight if the shock ram pressure equals the blast-wave ram pressure. If the ram pressure is about 3 times the typical blast-wave pressure, as expected for the encounter between the blast wave and a dense cloud (McKee & Cowie 1975; Hester et al. 1994), the line-of-sight depth is about 2 pc. Thus, the filament is a sheet seen edge-on (see Hester 1987), but it is a much less extreme case than the crisp filament known as the Spur (Raymond et al. 1988), and it does not require a ram pressure exceeding the pressure of the X-ray–emitting gas.

## 4. DISCUSSION

Benvenuti et al. (1980) and D'Odorico et al. (1980) analyzed the *IUE* spectra combined with Miller's optical spectrum. They found that a shock speed range of 80–130 km $s^{-1}$ provided a reasonable match to the spectrum and that carbon was severely underabundant. They attributed the UV continuum to H I two-photon emission with some evidence for molecular fluorescence emission. We find that a more extended range of shock speeds is needed to match the observations, primarily because of the combination of very high ionization states (O VI and O V) in the HUT data and the strong low-ionization lines in the optical spectrum. We find only weak evidence for depletion of C or Si onto grains. A 30% depletion fits the observations best, but it probably lies within the uncertainty. Comparison of the HUT and *IUE* spectra supports the identification of the continuum seen with *IUE* as H I two-photon emission. The strong airglow in the HUT spectrum makes it difficult to assess the possibility of a contribution from fluorescence.

Perhaps the most interesting question raised by the combined spectrum is the nature of the spread in shock velocity at the observed position. The list of possibilities includes (1) an order of magnitude density range in the preshock medium (and approximately constant ram pressure provided by the thermal pressure of the hot X-ray–emitting gas); (2) a complex flow pattern produced by dynamical instabilities; or (3) a well-developed thermal instability. A more exotic possibility is (4) large-density contrasts in the preshock gas produced by the saturated Alfvén wave turbulence in the cosmic-ray precursor invoked in diffusive shock models of cosmic-ray acceleration.

We consider the following hypotheses:

1.—*Clumpy Ambient Medium.* An order of magnitude density range within the 0.2 × 1 pc region viewed by HUT is a plausible hypothesis. Indeed, a larger density contrast between the X-ray–producing blast wave and the optical filament is already required. The density range could take the form of a large-scale gradient along the line of sight, or it

might be a collection of small clouds. The overall morphology and velocity structure of the Cygnus Loop optical filaments in this region is matched well by a large sheet with modest ripples and therefore modest density range (Hester 1987). A large-scale density gradient along the line of sight is therefore more likely than a swarm of small clouds.

2.—*Kelvin-Helmholtz or Richtmeyer-Meshkov Instability.* Dynamical instabilities can cause rapidly growing complex structure when a blast wave encounters a dense cloud, as in the numerical models of Klein, McKee, & Colella (1994), Stone, Xu, & Hardee (1997), or Jones & Kang (1993). Examples in the Cygnus Loop include the southeastern cloudlet (Fesen, Kwitter, & Downes 1992) and the small [O III] clouds seen in deep images of the northeast Cygnus Loop (Hester, Raymond, & Danielson 1986). The emission spectrum from such a complex flow has not been computed in detail. If the turbulence can mix hot and cold gas to small scales very rapidly, it might resemble a mixing layer model (Slavin, Shull, & Begelman 1993), but the emission of the shock itself is likely to overwhelm the emission from the subsequent equal pressure mixing of the flows. The spectral signatures of mixing layers would be strong UV emission in low-ionization lines or high UV/optical line ratios, and neither is seen.

3.—*Thermal Instability.* Much of the shock velocity range inferred above lies in the thermally unstable range above 150 km $s^{-1}$ (Chevalier & Imamura 1982; Innes, Giddings, & Falle 1987; Gaetz, Edgar, & Chevalier 1988). Other Cygnus Loop filaments that have been analyzed in detail, such as the Spur (Raymond et al. 1988), are very incomplete, meaning that the shock structure may not have had time to develop the secondary shocks that eventually form. There is no evidence for incompleteness at Miller's position 1, but the broad range of shock speeds makes it difficult to place limits on the completeness of the faster shocks. It is possible that the shock at Miller's position 1 has proceeded through several cycles and produced a chaotic structure with a broad range of shock conditions, although the rapid deceleration inferred for some nearby filaments (Hester et al. 1994) suggests that the shock speed does not remain in the unstable range for long. It is possible that a quasi–one-dimensional thermally unstable shock might produce a spectrum resembling that of a broad range of shock speeds, but Innes (1992) found that the time average of a one-dimensional thermally unstable 180 km $s^{-1}$ shock did not depart severely from that of a simple one-dimensional model.

4.—*Turbulent Cosmic-Ray Precursor.* Models of diffusive acceleration of cosmic rays by shock fronts involve a precursor where particles are trapped by the shock front and pitch angle scattering owing to Alfvén waves (Blandford & Eichler 1987). Saturated Alfvén turbulence suggests $\delta n/n \sim 1$ and shock speeds varying over a factor of $\sqrt{2}$. The shock speed range is at least twice this large. Thus, a cosmic-ray precursor seems unlikely to account for the observed range of shock speeds, but detailed predictions are not available.

In summary, while the FUV spectra, particularly the O VI seen with HUT, require a broad shock velocity range, we cannot yet differentiate among the different explanations for this range. A combination of high-velocity resolution and three-dimensional numerical simulations will be required to eliminate some of the possibilities.

This work was supported by NASA grant NAG 8-1074 to the Smithsonian Astrophysical Observatory and Contract NAS 5-27000 to Johns Hopkins University. Funding for the UIT project has been through the *Spacelab* Office at NASA under project 440-51. We are grateful to Nancy Levenson for providing Figure 2 and for measuring the [O III] fluxes from the projected apertures.

## REFERENCES

Allen, C. W. 1973, Astrophysical Quantities (3rd ed.; London: Athlone), 31
Benvenuti, P., Dopita, M., & D'Odorico, S. 1980, ApJ, 238, 601
Blair, W. P., Sankrit, R., Raymond, J. C., & Long, K. S. 1999, AJ, 118, 942
Blair, W. P., et al. 1991, ApJ, 379, L33
Blandford, R., & Eichler, D. 1987, Phys. Rep., 154, 1
Cardelli, J. A., Clayton, G. C., & Mathis, J. S. 1989, ApJ, 345, 245
Chevalier, R. A., & Imamura, J. N. 1982, ApJ, 261, 543
Cornett, R. H., et al. 1992, ApJ, 395, L9
Cox, D. P. 1972a, ApJ, 178, 143
———. 1972b, ApJ, 178, 159
———. 1972c, ApJ, 178, 169
Danforth, C. W., Cornett, R. H., Levenson, N. A., Blair, W. P., & Stecher, T. P. 2000, AJ, 119, 2319
D'Odorico, S., Benvenuti, P., Dennefeld, M., Dopita, M. A., & Greve, A. 1980, A&A, 92, 22
Dopita, M. A., & Sutherland, R. S. 1996, ApJS, 102, 161
Fesen, R. A., Kwitter, K. B., & Downes, R. A. 1992, AJ, 104, 719
Gaetz, T. J., Edgar, R. J., & Chevalier, R. A. 1988, ApJ, 329, 927
Hartigan, P., Raymond, J., & Hartmann, L. 1987, ApJ, 316, 323
Hester, J. J. 1987, ApJ, 314, 187
Hester, J. J., Raymond, J. C., & Blair, W. P. 1994, ApJ, 420, 721
Hester, J. J., Raymond, J. C., & Danielson, G. E. 1986, ApJ, 303, L17
Innes, D. E. 1992, A&A, 256, 660
Innes, D. E., Giddings, J. R., & Falle, S. A. E. G. 1987, MNRAS, 226, 67
Jones, A. P., Tielens, A. G. G. M., & Hollenbach, D. J. 1996, ApJ, 469, 740
Jones, A. P., Tielens, A. G. G. M., Hollenbach, D. J., & McKee, C. F. 1994, ApJ, 433, 797
Jones, T. W., & Kang, H. 1993, ApJ, 402, 560
Klein, R. I., McKee, C. F., & Colella, P. 1994, ApJ, 420, 213
Kriss, G. A. 1994, in ASP Conf. Ser. 61, Astronomical Data Analysis Software and System III, ed. D. R. Crabtree, R. J. Hanisch, & J. Barnes (San Francisco: ASP), 437
Kruk, J. W., Durrance, S. T., Kriss, G. A., Davidsen, A. F., Blair, W. P., & Espey, B. R. 1995, ApJ, 454, L1
Ku, W. H.-M., Kahn, S. M., Pisarski, R., & Long, K. S. 1984, ApJ, 278, 615
Levenson, N. A., et al. 1997, ApJ, 484, 304
Levenson, N. A., Graham, J. R., Hester, J. J., & Petre, R. 1996, ApJ, 468, 323
Levenson, N. A., Graham, J. R., Keller, L. D., & Matthew, J. 1998, ApJS, 118, 541
Long, K. S., Blair, W. P., Vancura, O., Bowers, C. W., Davidsen, A. F., & Raymond, J. C. 1992, ApJ, 400, 214
McKee, C. F., & Cowie, L. L. 1975, ApJ, 195, 715
Miller, J. S. 1974, ApJ, 189, 239
Miyata, E., Tsunemi, H., Pisarski, R., & Kissel, S. E. 1994, PASJ, 46, L101
Parker, R. A. R. 1967, ApJ, 149, 363
Raymond, J. C. 1979, ApJS, 39, 1
Raymond, J. C., Blair, W. P., Long, K. S., Vancura, O., Edgar, R. J., Morse, J., Hartigan, P., & Sanders, W. T. 1997, ApJ, 482, 881
Raymond, J. C., et al. 1980, ApJ, 238, 881
Raymond, J. C., Hester, J. J., Blair, W. P., Fesen, R. A., & Gull, T. R. 1988, ApJ, 324, 869
Scalo, J. M. 1977, A&A, 55, 253
Shull, P., Jr., Dyson, J. E., Kahn, F. D., & West, K. A. 1985, MNRAS, 212, 799
Slavin, J. D., Shull, J. M., & Begelman, M. C. 1993, ApJ, 407, 83
Stecher, T. P., et al. 1992, ApJ, 395, L1
Stone, J., Xu, J., & Hardee, P. 1997, ApJ, 483, 136
Szentgyorgyi, A. H., Raymond, J. C., Hester, J. J., & Curiel, S. 2000, ApJ, 529, 279
Vancura, O., Blair, W. P., Long, K. S., & Raymond, J. C. 1992a, ApJ, 394, 158
Vancura, O., et al. 1992b, ApJ, 401, 220